Analysis of reflections in GNSS radio occultation measurements using the phase matching amplitude

Thomas Sievert[1], Joel Rasch[2], Anders Carlström[3], and Mats I. Pettersson[1]

[1]Blekinge Institute of Technology, Karlskrona, Sweden
[2]Molflow, Gothenburg, Sweden
[3]RUAG Space AB, Gothenburg, Sweden

Correspondence to: Thomas Sievert (thomas.sievert@bth.se)

Abstract. It is well-known that in the presence of super-refractive (SR) layers in the lower troposphere inversion of GNSS radio occultation (RO) measurements using the Abel transform yields biased refractivity profiles. As such it is problematic to reconstruct the true refractivity from the RO signal. Additional information about this lower region of the atmosphere might be embedded in reflected parts of the signal. To retrieve the bending angle, the phase matching operator can be used. This operator produces a complex function of the impact parameter, and from its phase we can calculate the bending angle. Instead of looking at the phase, in this paper we focus on the function's amplitude. The results in this paper show that the signatures of surface reflections in GNSS RO measurements can be significantly enhanced when using the phase matching method by processing only an appropriately selected segment of the received signal. This signature enhancement is demonstrated by simulations and confirmed with ten hand-picked MetOp-A occultations with reflected components. To validate that these events show signs of reflections, radio holographic images are generated. Our results suggest that the phase matching amplitude carries information that can improve the interpretation of radio occultation measurements in the lower troposphere.

1   Introduction

GNSS radio occultation (RO) is a technique used for sounding the Earth's atmosphere. Assuming spherical symmetry of the atmosphere, the bending angles of GNSS signals passing through the atmosphere can be found and assimilated into numerical weather prediction (NWP) systems. The bending angle measurements contain valuable information due to their relation to the atmosphere's refractivity, which can yield information about humidity, temperature and pressure (e.g., Kursinski et al., 2000; Yunck et al., 2000). The geometry of transmitter, Earth, and receiver, as well as the short wavelength of the signals, result in a measurement with high vertical resolution. In many RO events, the instrument in orbit receives reflected components of the signal as well as direct ones. Boniface et al. (2011) have shown that reflected signals contain meteorological information. A method to detect these reflected components was suggested by Hocke et al. (1999) and has later been used on real data and shown to work (e.g., Beyerle et al., 2002; Pavelyev et al., 2002). This method uses a radio hologram generated by subtracting a ray traced reference field from the received signal. An effort to flag occultation events where reflections are present is described by Cardellach and Oliveras (2016), based on a supervised learning approach classifying such radio holographic images. It has since been employed by the Radio Occultation Meteorology Satellite Application Facility (ROM SAF) to flag millions of

occultation events. Cardellach and Oliveras also investigate whether knowledge of these reflections can improve the quality of RO data, however Healy (2015) concludes that a binary reflection flag is probably inappropriate for assimilation purposes. Gorbunov (2016) proposes a technique based on the canonical transform to retrieve bending angle profiles of reflected rays, and achieves a good agreement with the ROM SAF database.

5   When processing a RO signal, we use the phase matching (PM) operator (Jensen et al., 2004), which outputs a complex function of impact parameter whose phase is proportional to the signal's bending angle. Although the amplitude of this function may contain valuable information as well, it has not been appropriately investigated.

In this paper, we compare the phase matching amplitudes of simulated measurements to real measurements made by the GRAS instrument aboard MetOp-A. We demonstrate signatures corresponding to surface reflections, and truncate the received

10   signal to distinguish them from the much stronger signatures of the direct components. We motivate this truncation using simulated data and a simple geometric model for where reflected components are expected to appear in the signal, and we provide radio holographic images as a means of validation. Finally we discuss the difference in structure between simulated and real signals, as well as the potential future uses of the PM amplitude. In the appendix we motivate that the PM operator admits reflected signal components.

15   **2   Phase matching**

Jensen et al. define PM as an operator that transforms a complex signal of time $u(t)$ to impact parameter space:

$$U(a) = \int_{t_{min}}^{t_{max}} u(t) \exp\left(-ik_0 S(t,a)\right) dt \qquad (1)$$

Here, k_0 is the wave number in vacuum associated to the carrier frequency of the GNSS transmitter, $S(t,a)$ is the optical path length of a model ray path, and a is impact parameter. The derivative of $arg(U(a))$ with respect to a is proportional to the

20   bending angle. As this integral is defined for any impact parameter a, it is important to determine at which a the function does not contain relevant information anymore. The lowest a (which we call a_{min} in this paper) is usually around 2.1 km above the radius of the Earth's curvature, which corresponds to a surface refractivity of approximately 330 refractive units. To make sure that all information in the signal is mapped to impact parameter space, we compute the U for impact parameter values going all the way to the Earth's surface. This also ensures that we include reflected rays in the U function. It is not obvious that the PM

25   method should work for reflected rays, as the geometrical model ray path is constructed for a direct ray, but in the appendix it is shown that the standard phase matching technique works perfectly well to use on reflected rays, provided the Earth surface is smooth.

3   A model for reflected rays

In Fig. 1 we use two real MetOp-A measurements to demonstrate that some of the features we see in the amplitude for the

30   complex function U are caused by reflections. By overlaying the predicted straight line tangent altitude (SLTA) for the direct

rays (blue line), and reflected rays (red line) as a function of impact height the reflection is illustrated. To generate these SLTA plots we use the co-located ECMWF refractivity profiles. The black lines show the amplitude of the U function when passing segments of the signal to the PM operator using a 10 km sliding window. The relationship between reflected bending angle and impact parameter is well-known (see e.g., Pavelyev et al., 2011; Gorbunov, 2016) and can be described as

$$5 \quad \alpha(a) = -2a \int_{R_E n(R_E)}^{\infty} \frac{1}{\sqrt{r^2 n^2 - a^2}} \frac{d \ln n}{dr} dr - \pi + 2 \arcsin \left(\frac{a}{R_E n(R_E)} \right), \qquad (2)$$

where α is the bending angle, R_E the Earth radius of curvature, and n the refractive index as a function of radius. The bending angle of a direct ray is given by the same expression without the last two terms. The integral can be evaluated numerically using a number of techniques, and we employ the method described in (Rasch, 2014). The SLTA for fixed values of the LEO and GNSS orbital radii is given by

$$10 \quad SLTA = \frac{r_L r_G \sin \theta}{\sqrt{r_L^2 + r_G^2 - 2 r_L r_G \cos \theta}} - R_E \qquad (3)$$

Where r_L and r_G are the LEO and GNSS orbit radii, and θ is the separation angle between the satellites, given by

$$\theta = \pi + \alpha - \arcsin \left(\frac{a}{r_L} \right) - \arcsin \left(\frac{a}{r_G} \right) \qquad (4)$$

4 MetOp-A data

The data from occultation events is collected from the COSMIC Data Analysis and Archive Center (CDAAC) web interface,
15 specifically day 2007.274 with the metopa2016 designation, indicating reprocessed measurements from MetOp-A. The signal amplitude, excess phase and orbit data needed for PM are all found in the atmPhs files. In these files, the orbit coordinates are given with the Earth's center of mass as the point of origin. To fulfil the assumption of local spherical symmetry, we translate the coordinates so that they instead consider the center of curvature of the Earth at the occultation point. This is done by collecting translation data from the corresponding atmPrf files. As the atmPrf files contain bending angle and impact height
20 values, these were used to control the accuracy of the PM implementation.

    For simulating a GNSS signal as it passes through the atmosphere, a wave optics propagator (WOP) is used with the multiple phase screen technique (see e.g., Benzon et al., 2003; Benzon and Gorbunov, 2012; Rasch, 2014). The WOP uses a simpler, two-dimensional geometry where the GNSS transmitter is stationary. To achieve an occultation that matches the three-dimensional data in the atmPhs files, the GNSS transmitter position is set at a distance corresponding to the mean value of
25 the distance between the center of curvature and the actual GNSS position. Similarly, the receiver satellite orbit is assigned a constant radius. To determine the length of the orbit (how deep the occultation goes), the minimum and maximum separation angles between transmitter and receiver are computed and used. These values can be modified to simulate an occultation event

tracked to a lower SLTA. For an atmosphere, the high-resolution, co-located refractivity profile from ECMWF also provided by CDAAC is used (echPrf files). These profiles do not go all the way to the ground - the last bit is extrapolated linearly. To simulate surface reflections, we set the electromagnetic field to 0 on all parts of the phase screens that lie inside the Earth. Although it is not clear whether this method has a solid physical basis it appears to give quite accurate results, and is routinely
5 used in WOP simulations (Gorbunov, 2016; Levy, 2000).

As a frame of reference, radio holographic images are produced by constructing a "beating function" from the excess phase, signal amplitude and a reference field, and using the short-time fast Fourier transform with a sliding window, similar to Boniface et al. (2011).

5 Surface reflections

10 In the lowest part of an occultation (SLTA around -80 km, impact height around 2.1 km), where the signal becomes shadowed by the Earth, the magnitude of U also decreases. The lowest direct ray becomes diffracted by the Earth's surface and gradually decreases in magnitude over a region corresponding to the Fresnel zone size, which is seen clearly in simulated data, and frequently less clearly in measured data. This transition occurs over a few hundred meters (Kursinski et al., 2000), around $SLTA_{min}$, and a_{min}, whose values are determined by the Earth radius, and the refractive index at ground. Quite often when
15 the signal is lost at an SLTA value that is substantially higher than $SLTA_{min}$ we see a spike in $|U|$ around a_{min}. This spike is most easily explained as a reflection. If tracking of the signal goes all the way to the surface this spike overlaps with the direct signal and is obfuscated. In Fig. (1) we see that the reflected signal and the direct signal coincide around a_{min} (approximately at 2.1 km). For the left panel this occurs at the deepest SLTA (around -90 km), and for the right panel this again occurs around -90 km, but the deepest part of the signal goes to -150 km, and occurs at an impact height around 2.8 km, which corresponds
20 to a region of strong refractivity gradients. The value for SLTA where the direct and reflected signals join we call $SLTA_{min}$. By cutting the signal well above $SLTA_{min}$ at an SLTA around -50 km it is clear from Fig. (1) that we would only keep the upper parts of the reflected and direct signals, and completely remove the signal parts containing the diffraction signature around a_{min}, and the deep signals caused by strong refractivity gradients. In Fig. (2) we can see the same thing. The abrupt decrease in $|U|$ around an impact height of 2.1 km (at a_{min}) corresponds to the point where the reflected and direct signals
25 join, and the direct signal becomes diffracted. By cutting the signal at -65 km the lower parts of the reflected and direct signals are removed, and the reflection signature becomes clearly separated from the direct signal.

The nature of the PM operator is such that sharp discontinuities in the signal introduce significant noise in the $|U|$ function. To avoid these, we taper the signals using a one-sided Tukey window (Bloomfield, 2004). In the case of the sliding window used in Fig. (1), we use a two-sided window. The noise generated by omitting any sort of tapering is demonstrated in Fig. (2),
30 where the simulated signal ends abruptly.
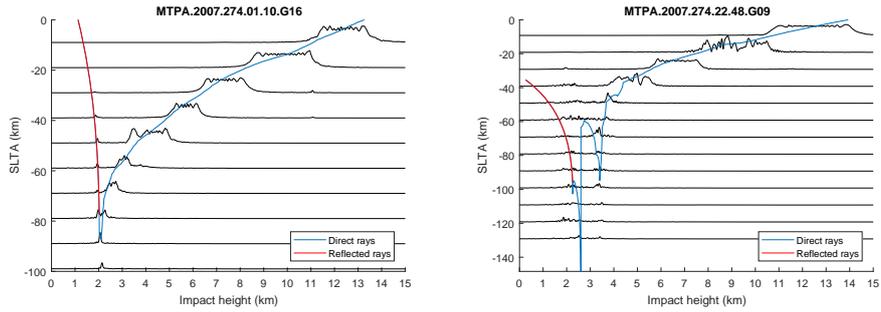
Figure 1. Using a sliding window for the signal yields PM amplitudes that correspond to the reflection model. Left shows a case with weak refractive gradients, right shows a case with strong refractive gradients.
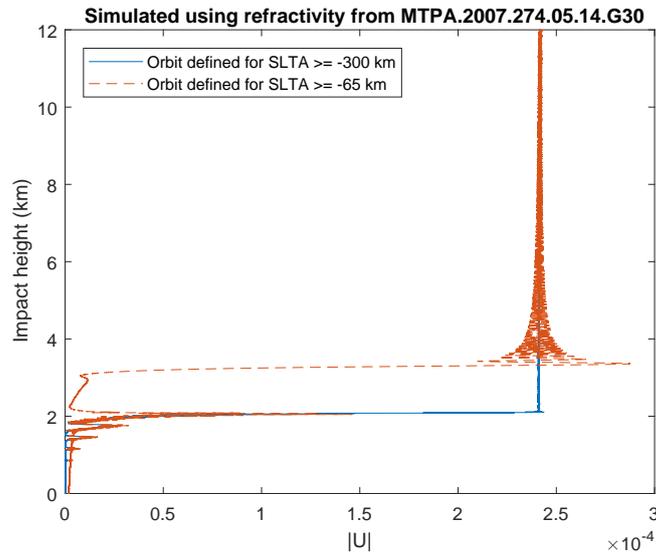
Figure 2. $|U|$ for a simulated signal that is propagated to a shallow orbit, and one that is propagated to a deeper orbit (blue). For illustration the truncated signal is not tapered, producing dramatic oscillations around 4 km.

6 Results

We present ten cases where PM is performed on real signals alongside their simulated counterparts based on ECMWF's co-located refractivity profiles. These cases are classified in categories 1 through 4 based on the sharpest gradient above 100 m, in the same manner as the reference dataset from ECMWF (Healy, 2012), where category 4 have the sharpest gradients. Overall, the structure of $|U|$ is similar to that of a step function, both in simulations and using real data. By truncating the signals at an appropriate SLTA we can distinguish previously hidden reflection spikes in $|U|$. For this study we pick the altitude of truncation qualitatively. Figures (3) through (12) show the received signal (first from the left), $|U|$ for a simulated signal (second from the

left), $|U|$ for the received signal (third from the left), and a radio hologram generated from the signal (fourth from the left). The first, second and third plot from the left are color coded so that the blue plots describe the complete signals, and the red plots describe the truncated signals. All the truncated signals have been tapered using the aforementioned Tukey window to avoid introducing additional noise.

5   Simulations on cases classified as category 3 and 4 - shown in Fig. (8) through (12) - give rise to a sharp, negative spike at an impact height corresponding to the sharp gradient in the refractivity profile. This structure cannot be found in the real data. Moreover, the real data shows a high level of noise that is not found in simulated data.

    We note that there are peculiar oscillating structures in the real data. Particularly in Fig. (4) at 6 km, Fig. (7) at 4 and 6 km, Fig. (8) at 7.5 km, Fig. (11) at 5 and 9 km, and in Fig. (12) at 5 and 9 km. These oscillating structures are not found in the 10 simulated data.

    While these ten hand-picked cases all clearly contain reflected components, there are several measurements in which the reflected parts cannot be distinguished. This is typically either because the measurement was not deep enough, or because $|U|$ was too noisy. When the measurements are sufficiently deep, and the noise level of $|U|$ is low, there are very clear reflection spikes. This is corroborated by the radio holographic images, who also show very clear reflection patterns in those cases. The 15 bright yellow trail around 0 Hz is the direct signal, whereas the more faint trail going off to negative frequencies (and appearing again at positive frequencies due to aliasing) is the reflected signal. The signal has everywhere been divided by the average signal amplitude in the window. This is done to make the reflection and the direct signal for low SLTA stand out against the strong signature of the direct signal for high SLTA. This also often causes the hologram to give the appearance of containing strong broadband noise for low SLTA, but it is actually the amplification of weak noise.
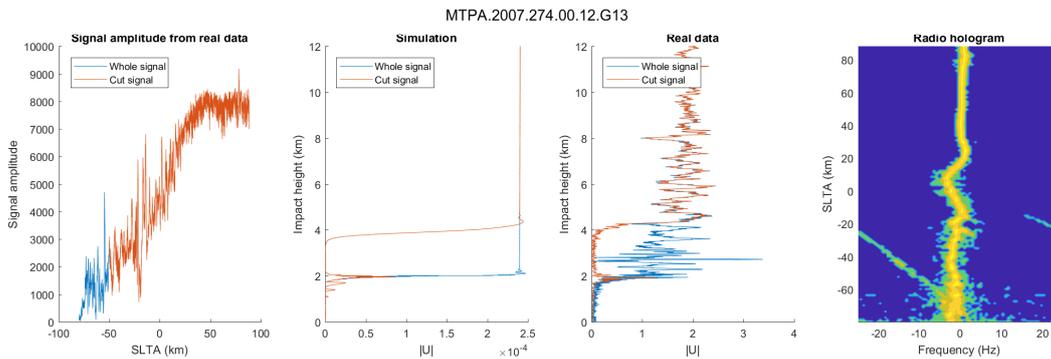
Figure 3. An event classified into category 1. $SLTA_{min}$ is at approximately -73 km, and the signal is truncated at $SLTA = -50$ km.
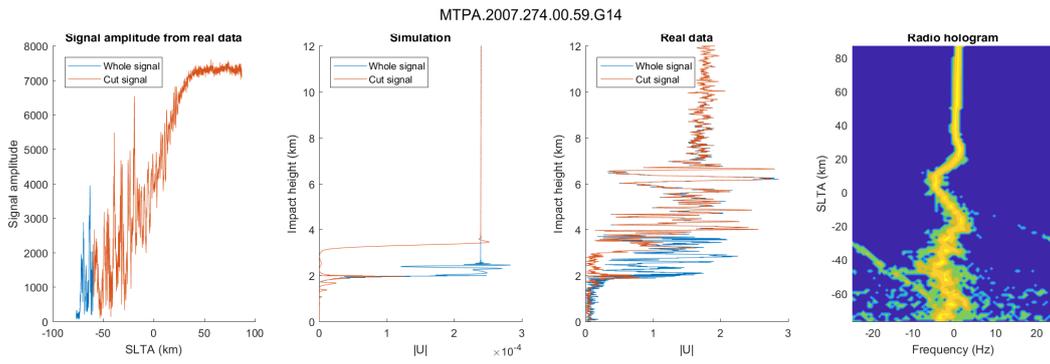
Figure 4. An event classified into category 1. $SLTA_{min}$ is at approximately -73 km, and the signal is truncated at $SLTA = -60$ km.
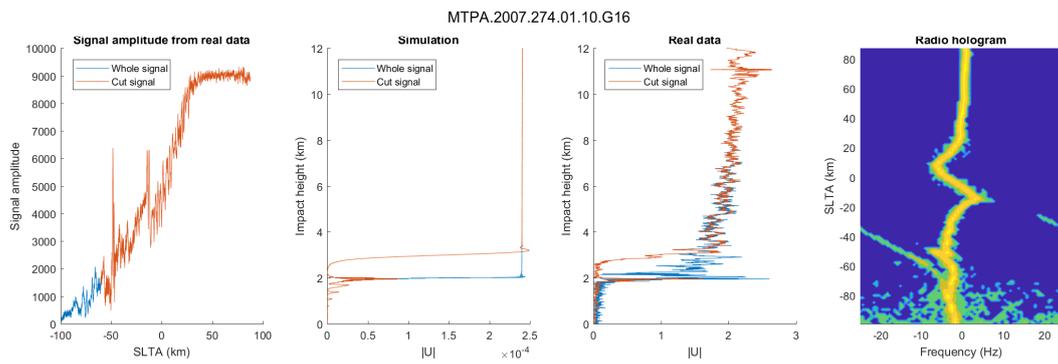
Figure 5. An event classified into category 1. $SLTA_{min}$ is at approximately -86 km, and the signal is truncated at $SLTA = -60$ km.
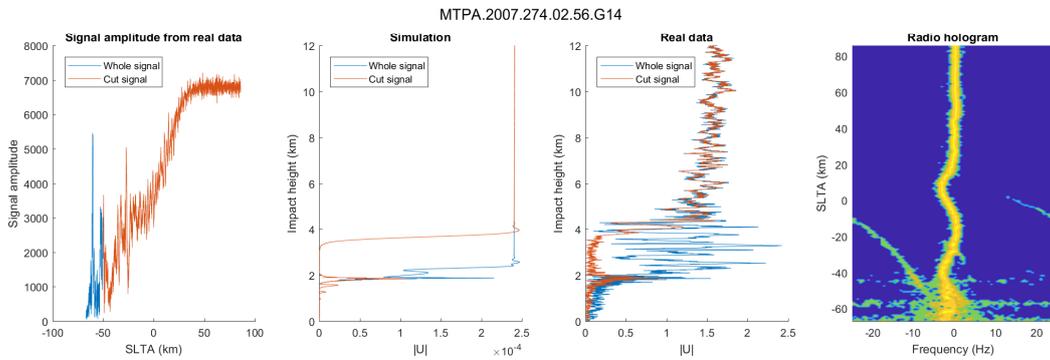
Figure 6. An event classified into category 1. $SLTA_{min}$ is at approximately -65 km, and the signal is truncated at $SLTA = -50$ km.
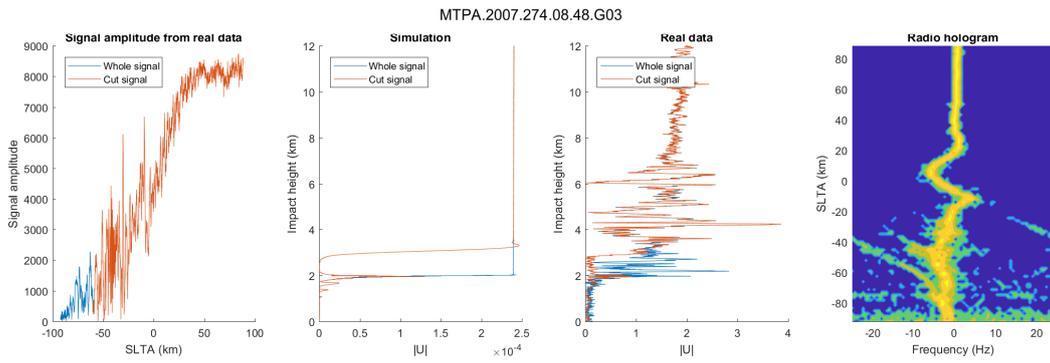
Figure 7. An event classified into category 1. $SLTA_{min}$ is at approximately -72 km, and the signal is truncated at $SLTA = -60$ km.
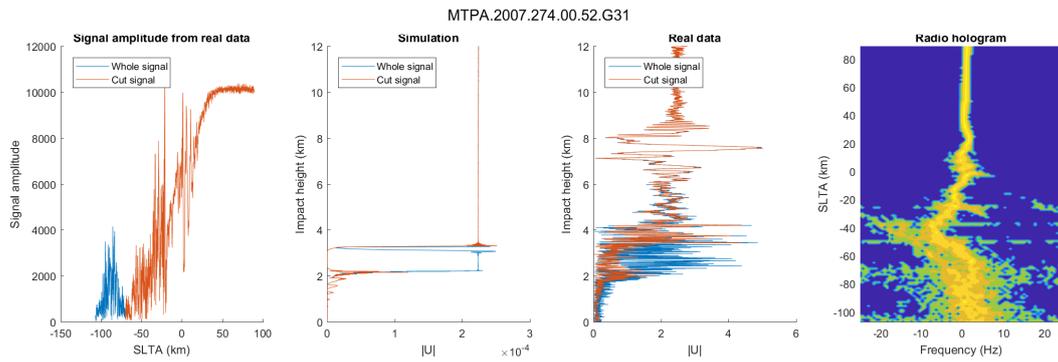
Figure 8. An event classified into category 3. $SLTA_{min}$ is at approximately -87 km, and the signal is truncated at $SLTA = -70$ km.
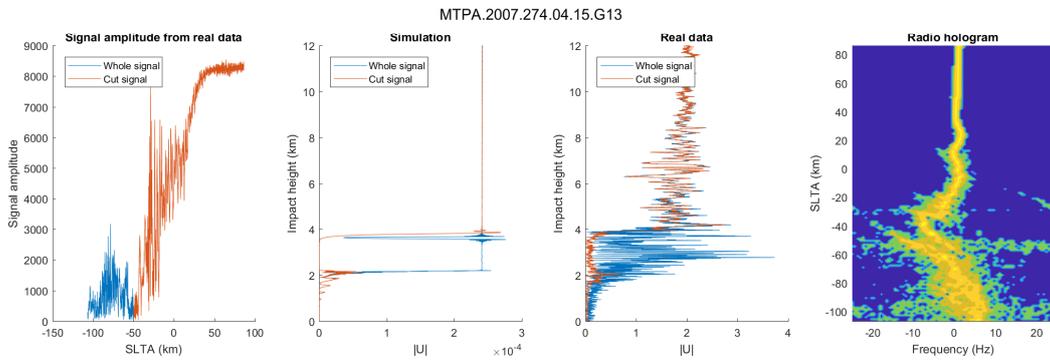
Figure 9. An event classified into category 3. $SLTA_{min}$ is at approximately -84 km, and the signal is truncated at $SLTA = -50$ km.
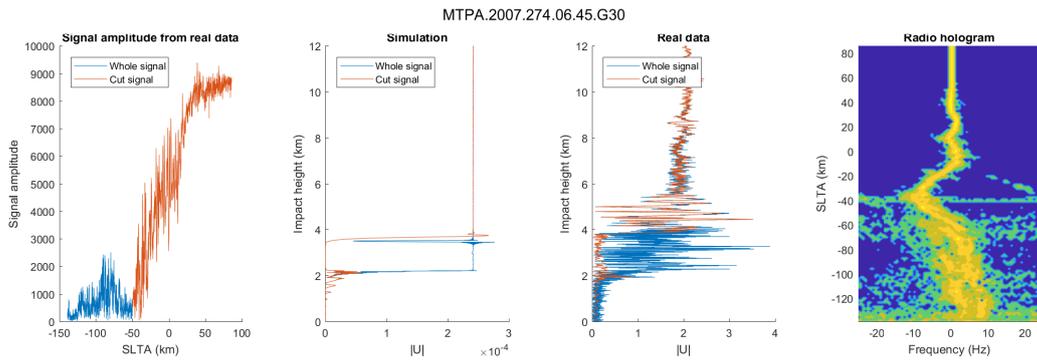
Figure 10. An event classified into category 3. $SLTA_{min}$ is at approximately -85 km, and the signal is truncated at $SLTA = -50$ km.
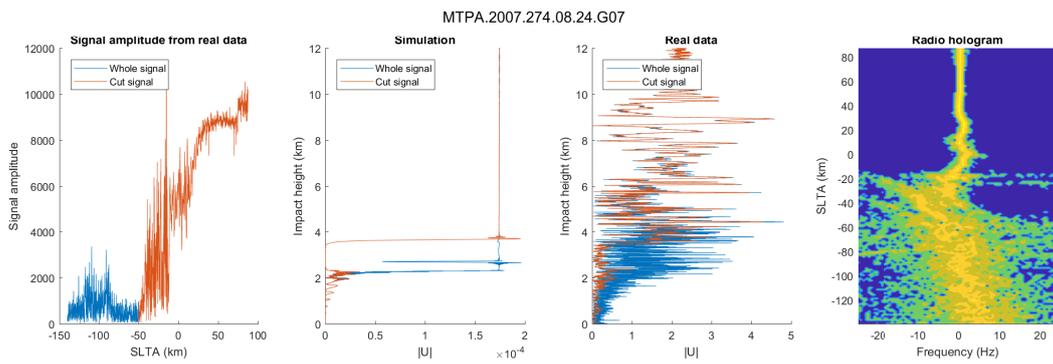
Figure 11. An event classified into category 3. $SLTA_{min}$ is at approximately -99 km, and the signal is truncated at $SLTA = -50$ km.
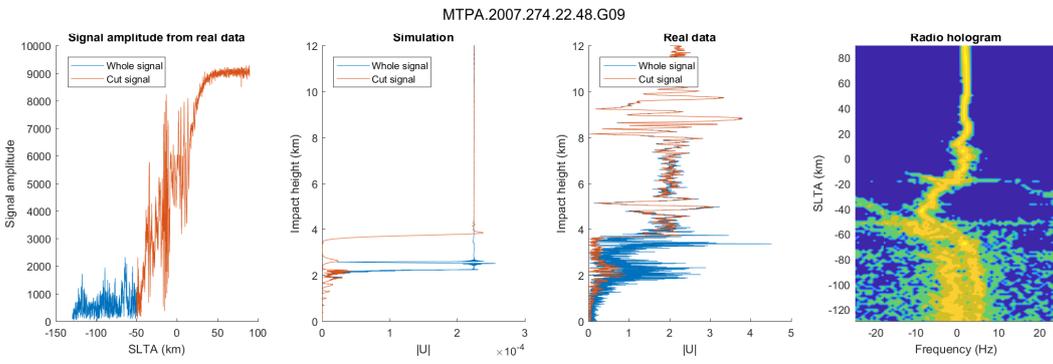
Figure 12. An event classified into category 4. $SLTA_{min}$ is at approximately -103 km, and the signal is truncated at $SLTA = -50$ km.

7 Conclusions

The results in this paper show that the signatures of surface reflections in GNSS RO measurements can be significantly enhanced when using the PM method by processing only an appropriately selected segment of the received signal. We can then identify reflection signatures even in cases where they are normally obscured by the direct signal's influence on the PM amplitude. This signature enhancement is demonstrated by simulations and confirmed with MetOp-A measurements. For further validation of the reflections, radio holographic images are provided for comparison. For the cases presented, clear and sharp reflection spikes in the PM amplitude are corroborated with clear reflection patterns in their corresponding radio holograms. Weaker or less distinct spikes have more noise in their corresponding radio holograms.

The events containing reflected signals presented here are hand-picked to illustrate that the approach can be useful for identifying reflections in real measurements. There are still questions that can only be answered by larger volumes of data, e.g. if the PM amplitude can possibly be used to retrieve information related to the reflected signal. Furthermore we observe that the reflection spikes vary greatly in shape. Additionally, simulated reflection spikes always occur very close to the surface impact parameter, however in real measurements this is not always the case. The reason for these variabilities needs to be investigated. At this point we have only analyzed events over water, since we expect those reflections to be much clearer and numerous compared to events over land.

When comparing the PM amplitudes of real and simulated signals, some interesting discrepancies were found. First, the characteristic dip in $|U|$ associated with a region of sharp gradient in the refractivity could not be identified in the real data, being completely drowned in noise, or simply not present. Second, the levels of noise in the $|U|$ function tends to increase close to the Earth surface. As no noise was added to the simulations, it is not clear if this is due to instrument noise, or atmospheric disturbances. Third, peculiar oscillatory features at quite distinct heights were seen in the real data but not at all in the simulated. These features are not understood at present, but it is likely that they have to do with horizontal gradients in the refractive index, and with aliasing of the reflected signal onto the direct signal due to low sampling rate. What horizontal gradients do to the PM amplitude has not been investigated, but it is likely that it will decrease the amplitude, and cause additional noise, perhaps resulting in these peculiar oscillations. Regarding the aliasing of reflected signals it is quite clearly seen in some of the radio holograms that the reflected signal is still strong when it has been aliased and again approaches the direct signal in frequency. This may cause a degradation of the PM method (the integral over the stationary phase point) at the specific impact height that belongs to the direct signal at the point where the direct and reflected aliased signal match in frequency.

8 Data availability

The data from occultation events is collected from the COSMIC Data Analysis and Archive Center (CDAAC) web interface, found at the URL http://cdaac-www.cosmic.ucar.edu/cdaac/index.html.

Appendix A: Phase matching for reflected rays

It is not obvious that the phase matching method should work for reflected rays without modifications, but we will show that it does, under the assumption of reflections taking place on a perfectly smooth surface. First we will review the method used for phase matching of direct (non-reflected) rays, and then we will show that the result is the same for reflected rays. For the full details of the phase matching method the reader is referred to (Jensen et al., 2004).

A1 Direct rays

Under the assumption of spherically symmetric atmosphere we can use Bouger's rule

$$rn(r)\sin\phi = a \tag{A1}$$

where r is the distance from the Earth centre of curvature, n the refractive index, ϕ the angle the ray makes with the radial vector, and a the impact parameter. A ray is emitted from the GNSS satellite (at r_G) with angle ϕ_G, being smaller than π. The ray makes its closest approach to the Earth when $\phi = \pi/2$. The ray then exits the atmosphere and is received at the LEO satellite (at r_L) with the angle ϕ_L. The total bending of the ray (measured positive towards the Earth) is given by the bending angle

$$\alpha(a) = -2a\int\limits_{a}^{\infty} \frac{1}{\sqrt{r^2n(r)^2 - a^2}}\frac{d\ln n}{dr}dr \tag{A2}$$

The optical path length for the ray is given by the integral over the refractive index along the path of the ray

$$S = \int n(r)ds \tag{A3}$$

Where the term ds is an infinitesimal length along the ray. Under the spherical symmetry assumption the integral can be recast in a very attractive form, viz

$$S(t,a) = \sqrt{r_L(t)^2 - a^2} + \sqrt{r_G(t)^2 - a^2} - 2a^2\int\limits_{a}^{\infty} \frac{1}{\sqrt{r^2n(r)^2 - a^2}}\frac{d\ln n}{dr}dr - 2\int\limits_{a}^{\infty}\sqrt{r^2n(r)^2 - a^2}\frac{d\ln n}{dr}dr \tag{A4}$$

The last term is connected to the bending angle in the following way

$$\int\limits_{a}^{\infty}\alpha(a')da' = -2\int\limits_{a}^{\infty}\sqrt{r^2n(r)^2 - a^2}\frac{d\ln n}{dr}dr \tag{A5}$$

Using also the definition for the bending angle (eq. A2) we can write

$$S(t,a) = \sqrt{r_L(t)^2 - a^2} + \sqrt{r_G(t)^2 - a^2} + \alpha(a)a + \int_a^\infty \alpha(a')da' \tag{A6}$$

The impact parameter is generally connected to a certain point in time, and certain values for r_L and r_G, in a complicated way. Whatever this connection may be the angles in the system must fulfill

5 $$\theta(t) + \phi_G + \phi_L - \pi = \alpha \tag{A7}$$

Where θ is the separation angle between the satellites. We can rewrite this using geometry

$$\theta(t) + \arcsin(a/r_L(t)) + \arcsin(a/r_G(t)) - \pi = \alpha \tag{A8}$$

For every value of a there will be a corresponding value for t. In that sense one could write the optical path length as a function of t only, viz

10 $$S(t) = \sqrt{r_L(t)^2 - a(t)^2} + \sqrt{r_G(t)^2 - a(t)^2} + \alpha(a(t))a(t) + \int_{a(t)}^\infty \alpha(a')da' \tag{A9}$$

In the phase matching method we perform an integral for each value of a given impact parameter a_g where we wish to find the bending angle. The signal is given by

$$u(t) = |u(t)| \exp(ikS(t)) \tag{A10}$$

where k_0 is the wavenumber, and $i = \sqrt{-1}$. We subtract a geometrical model for the ray and form an integral as

15 $$U(a_g) = \int_{t_0}^{t_E} |u(t)| \exp(ik(S(t) - S_g(t, a_g))) \tag{A11}$$

Where the geometrical ray is given by

$$S_g(t, a_g) = \sqrt{r_L(t)^2 - a_g^2} + \sqrt{r_G(t)^2 - a_g^2} + a_g\left(\theta(t) + \arcsin(a_g/r_L(t)) + \arcsin(a_g/r_G(t)) - \pi\right) \tag{A12}$$

The integral will get its main contribution from the point where there is a stationary phase point, characterized by

$$\frac{d}{dt}(S(t) - S_g(t, a_g)) = 0 \tag{A13}$$

The time derivative of S is given by

$$\frac{dS}{dt} = \frac{1}{r_L(t)}\frac{dr_L}{dt}\sqrt{r_L(t)^2 - a(t)^2} + \frac{1}{r_G(t)}\frac{dr_G}{dt}\sqrt{r_G(t)^2 - a(t)^2} + a(t)\frac{d\theta}{dt} \tag{A14}$$

Likewise, the time derivative of S_g is

$$\frac{dS_g}{dt} = \frac{1}{r_L(t)}\frac{dr_L}{dt}\sqrt{r_L(t)^2 - a_g^2} + \frac{1}{r_G(t)}\frac{dr_G}{dt}\sqrt{r_G(t)^2 - a_g^2} + a_g\frac{d\theta}{dt} \tag{A15}$$

5   Hence, the stationary phase point occurs where $a(t_g) = a_g$. At that point the difference in optical path length becomes

$$S(t_g) - S_g(t_g, a_g) = \int_{a_g}^{\infty} \alpha(a')da' \tag{A16}$$

And the integral is given by

$$U(a_g) = C(t_g)\exp\left(ik\int_{a_g}^{\infty}\alpha(a')da'\right) \tag{A17}$$

Where $C(t_g)$ is an amplitude factor depending on the signal amplitude and phase in the region around the stationary phase
10   point. The bending angle as a function of impact parameter is thus found by taking the derivative of the phase of the function
U with respect to a_g, i.e.

$$\alpha(a_g) = -\frac{1}{k}\frac{d\angle U(a_g)}{da_g} \tag{A18}$$

A2   Reflected rays

For rays suffering reflection the Bouger's rule still applies, but the ray never reaches the point where $\phi = \pi/2$. Instead the ray
15   is reflected at the point where $r = R_E$, where R_E is the Earth radius of curvature. Using the definition $R_E n(r_E) = a_E$ we find
the angle the ray makes with the radial vector at reflection to be

$$\phi_E = \arcsin\left(\frac{a}{a_E}\right) \tag{A19}$$

Here we naturally assume that $a < a_E$, otherwise the ray would never reach the surface and be reflected. Since we assume the
surface to be completely smooth, the radial vector is parallel to the surface normal, and since the incidence angle with respect

to the surface normal is equal to the reflected ray angle with respect to the surface normal, we find that the ray angle after reflection is

$$\phi'_E = \pi - \phi_E \tag{A20}$$

We conclude that the ray suffers a negative bending of π radians due to the reflection. The total bending angle for a reflected ray is therefore given by

$$\alpha(a) = -2a \int\limits_{a_E}^{\infty} \frac{1}{\sqrt{r^2 n(r)^2 - a^2}} \frac{d\ln n}{dr} dr - \pi + 2\phi_E \tag{A21}$$

The integral for the optical path length becomes more complicated (although the derivation is straightforward)

$$S(t,a) = \sqrt{r_L(t)^2 - a^2} - \sqrt{a_E^2 - a^2} + \sqrt{r_G(t)^2 - a^2} - \sqrt{a_E^2 - a^2} - 2a^2 \int\limits_{a_E}^{\infty} \frac{1}{\sqrt{r^2 n(r)^2 - a^2}} \frac{d\ln n}{dr} dr - 2 \int\limits_{a_E}^{\infty} \sqrt{r^2 n(r)^2 - a^2} \frac{d\ln n}{dr} dr \tag{A22}$$

Taking the time derivative of this expression leads to the very same expression as Eq. A14. Hence, the stationary phase point again occurs where $a(t_g) = a_g$. At this point we have

$$S(t_g) - S_g(t_g, a_g) = -2\sqrt{a_E^2 - a_g^2} + a_g \pi - 2a_g \arcsin\left(\frac{a_g}{a_E}\right) - 2 \int\limits_{a_E}^{\infty} \sqrt{r^2 n(r)^2 - a_g^2} \frac{d\ln n}{dr} dr \tag{A23}$$

This is the term that appears in the phase of the phase matching function $U(a_g)$. Taking the derivative with respect to a_g leads to

$$\frac{d}{da_g}\left(S(t_g) - S_g(t_g, a_g)\right) = -2a_g \int\limits_{a_E}^{\infty} \frac{1}{\sqrt{r^2(r)n^2 - a_g^2}} \frac{d\ln n}{dr} dr + \pi - 2\arcsin\left(\frac{a_g}{a_E}\right) \tag{A24}$$

Which is the bending angle for a reflected ray as given in Eq. (A21) Consequently the phase matching method works in the exact same way for direct and reflected rays. It should be stressed that these derivations are only valid when the Earth surface can be considered smooth. When the surface is not smooth the incoming ray will change impact parameter upon reflection. Due to this the expression for the optical path length becomes a function of the old and new impact parameter, and the simple geometrical ray model used in the phase matching method cannot lead to a stationary phase point. This is basically a case of multipath in the impact parameter domain. It may be argued though that this is of little consequence for real measurements

since the occultation measuring instrument will not record signals that deviate too strongly from direct rays, as they quite rapidly become heavily Doppler shifted with increasing reflection angle. For this reason reflected signals will only be seen at impact parameters that are very close to the value at the Earth surface. These rays are of grazing incidence, and under such circumstances the surface may always be considered as flat (Beekmann and A, 1963).

5   *Author contributions.* J. Rasch, T. Sievert, A. Carlström and M. I. Pettersson designed the study and T. Sievert performed the simulations and processing. T. Sievert prepared the manuscript with contributions from all co-authors. J. Rasch performed the calculations for the reflection model and wrote the appendix.

Acknowledgements. This research was supported by The Swedish National Space Board and The Knowledge Foundation (KKS).

References

Beekmann, P. and A, S.: The Scattering of Electromagnetic Waves from Rough Surfaces, International Series of Monographs on Electromagnetic Waves, Pergamon Press, 1963.

Benzon, H. H. and Gorbunov, M. E.: Description of a wave propagator and radio occultation simulations, Tech. rep., EUMETSAT, 2012.

5 Benzon, H. H., Nielsen, A. S., and Olsen, L.: An atmospheric wave optics propagator - theory and application, Scientific report 03-01, Danish Meteorological Institute, 2003.

Beyerle, G., Hocke, K., Wickert, J., Schmidt, T., Marquardt, C., and Reigber, C.: GPS radio occultations with CHAMP: A radio holographic analysis of GPS signal propagation in the troposphere and surface reflections, Journal of Geophysical Research: Atmospheres, 107, doi:10.1029/2001JD001402, 2002.

10 Bloomfield, P.: Fourier analysis of time series: an introduction, John Wiley & Sons, 2004.

Boniface, K., Aparicio, J., and Cardellach, E.: Meteorological information in GPS-RO reflected signals, Atmospheric Measurement Techniques, 4, 1397–1407, doi:10.5194/amt-4-1397-2011, 2011.

Cardellach, E. and Oliveras, S.: Assessment of a potential reflection flag product, ROM SAF Report 23, Radio Occultation Meteorology Satellite Application Facility, www.romsaf.org, 2016.

15 Gorbunov, M.: Development of wave optics code for the retrieval of bending angle profiles for reflected rays, ROM SAF Visiting Scientist Report 27, Radio Occultation Meteorology Satellite Application Facility, www.romsaf.org, 2016.

Healy, S.: Optimising Tracking Strategies for Radio Oc-cultation. Task 1-the profile dataset, Tech. rep., ECMWF/EUMETSAT, 2012.

Healy, S.: The use of the GPS radio occultation reflection flag for NWP applications, ROM SAF Visiting Scientist Report 22, Radio Occultation Meteorology Satellite Application Facility, www.romsaf.org, 2015.

20 Hocke, K., Pavelyev, A. G., Yakovlev, O. I., Barthes, L., and Jakowski, N.: Radio occultation data analysis by the radioholographic method, Journal of Atmospheric and Solar-Terrestrial Physics, 61, 1169–1177, doi:10.1016/S1364-6826(99)00080-2, 1999.

Jensen, A. S., Lohmann, M. S., Nielsen, A. S., and Benzon, H.-H.: Geometrical optics phase matching of radio occultation signals, Radio science, 39, doi:10.1029/2003RS002899, 2004.

Kursinski, E. R., Hajj, G. A., Leroy, S. S., and Herman, B.: The GPS radio occultation technique, Terrestrial, Atmospheric and Oceanic Sciences, 11, 53–114, 2000.

25 Levy, M.: Parabolic Equation Methods for Electromagnetic Wave Propagation, Electromagnetics and Radar Series, Institution of Electrical Engineers, 2000.

Pavelyev, A., Zhang, K., Matyugov, S., Liou, Y., Wang, C., Yakovlev, O., Kucherjavenkov, I., and Kuleshov, Y.: Analytical model of bistatic reflections and radio occultation signals, Radio Science, 46, 2011.

30 Pavelyev, A. G., Igarashi, K., Pavelyev, D. A., and Hocke, K.: Radioholographic method for observation of reflections from the {Earth}'s surface and of wave structures based on occultations, Journal of Communications Technology and Electronics, 47, 609–614, 2002.

Rasch, J.: Theory and Implementation of an End-to-End Radio Occultation Simulator, Technical Report, Earth and Space Sciences, no 10, Chalmers University of Technology, 2014.

Yunck, T. P., Liu, C.-H., and Ware, R.: A history of GPS sounding, Terrestrial, Atmospheric and Oceanic Sciences, 11, 1–20, 2000.